

Article

Combined Effect of Particle Reinforcement and T6 Heat Treatment on the Compressive Deformation Behavior of an A357 Aluminum Alloy at Room Temperature and at 350 °C

Sarah Johanna Hirsch * , Nadja Berndt , Thomas Grund  and Thomas Lampke 

Institute of Materials Science and Engineering, Chemnitz University of Technology, Erfenschlager Str. 73, 09125 Chemnitz, Germany; nadja.berndt@mb.tu-chemnitz.de (N.B.); thomas.grund@mb.tu-chemnitz.de (T.G.); thomas.lampke@mb.tu-chemnitz.de (T.L.)

* Correspondence: sarah-johanna.hirsch@mb.tu-chemnitz.de

Abstract: Solid state sintering of cast aluminum powders by resistance heating sintering (RHS), also known as spark plasma sintering or field-assisted sintering technique, creates a very fine microstructure in the bulk material. This leads to high performance material properties with an improved strength and ductility compared to conventional production routes of the same alloys. In this study, the mechanical behavior of an RHS-sintered age-hardenable A357 (AlSi7Mg0.6) cast alloy and a SiC_p/A357 aluminum matrix composite (AMC) was investigated. Aiming for high strength and good wear behavior in tribological applications, the AMC was reinforced with a high particle content (35 vol.%) of a coarse particle fraction ($d_{50} = 21 \mu\text{m}$). Afterwards, separated and combined effects of particle reinforcement and heat treatment were studied under compressive load both at room temperature and at 350 °C. At room temperature compression, the strengthening effect of precipitation hardening was about twice as high as that for the particle reinforcement, despite the high particle content. At elevated temperatures, the compressive deformation behavior was characterized by simultaneously occurring temperature-activated recovery, recrystallisation and precipitation processes. The occurrence and interaction of these processes was significantly affected by the initial material condition. Moreover, a rearrangement of the SiC reinforcement particles was detected after hot deformation. This rearrangement lead to a homogenized dispersion of the reinforcement phase without considerable particle fragmentation, which offers the potential for secondary thermo-mechanical processing of highly reinforced AMCs.

Keywords: aluminum cast alloy; AMC; compression; field-assisted sintering; heat treatment; hot deformation; mechanical properties; microstructure; SiC; solid-state sintering



Citation: Hirsch, S.J.; Berndt, N.; Grund, T.; Lampke, T. Combined Effect of Particle Reinforcement and T6 Heat Treatment on the Compressive Deformation Behavior of an A357 Aluminum Alloy at Room Temperature and at 350 °C. *Crystals* **2024**, *14*, 317. <https://doi.org/10.3390/cryst14040317>

Academic Editor: Marek Sroka

Received: 5 March 2024

Revised: 22 March 2024

Accepted: 27 March 2024

Published: 28 March 2024



Copyright: © 2024 by the authors. Licensee MDPI, Basel, Switzerland. This article is an open access article distributed under the terms and conditions of the Creative Commons Attribution (CC BY) license (<https://creativecommons.org/licenses/by/4.0/>).

1. Introduction

Al-Si-Mg cast alloys like A356 (AlSi7Mg0.3) and A357 (AlSi7Mg0.6) are used in many commercial engineering applications such as pistons, engine blocks, brake saddles, pumps, impellers and valve components [1]. Key factors for the use of these alloys are their high specific strength [1,2] and high toughness [2], particularly in their heat-treated conditions [3]. In addition, these alloys have an excellent castability [1], and due to the good fluidity in the molten state [4] they are popular candidates for additive manufacturing processes [4–6]. Nevertheless, the mechanical properties are significantly influenced by the manufacturing process, the resulting microstructure and the subsequent heat treatment. For example, the use of powder metallurgical processes can avoid potential problems of conventional cast structures, such as columnar grain growth and heterogeneous microstructures and thus gradual changes in the properties [2] due to thermal gradients and different local solidification velocities. In addition, the presence of the alloying elements Si and Mg allows for a significant improvement in strength due to precipitation hardening. The

precipitation sequence is generally accepted as [7–9]: super saturated solid solution → clusters → Guinier–Preston zones (GP I, coherent) → β'' (semi-coherent, needle-shaped) → β' (semi-coherent, rod-shaped) → β (incoherent). The highest strength can be achieved by a T6 heat treatment routine, i.e., solution annealing, water quenching and artificial ageing at elevated temperatures to achieve a high amount of finely dispersed β'' precipitates.

By reinforcing an aluminum alloy with a high ceramic particle content (≥ 20 vol.%, [10]) and particle sizes in the micrometer range, an aluminum matrix composite (AMC) with significantly improved wear behavior compared to the unreinforced monolithic aluminum matrix is created. There are many studies regarding the wear behavior of AMCs [11–16]. Besides this, the stiffness, strength, thermal stability and creep resistance are improved [10,17,18] by adding a ceramic reinforcement phase. Since up to about 60% of weight can be saved compared to grey cast iron, this material is predestined for tribologically stressed components, such as in brake discs [10,19]. Compared to wrought aluminum alloys hypereutectic and hypoeutectic (like AlSi7Mg alloys) are the predominantly used brake disc matrix materials [19], and (particulate) SiC (abbreviated: SiC_p) is the most commonly used reinforcement phase [19].

In recent decades, the mechanical behavior of AMCs under compression has been extensively studied. Mondal et al. [20] and Ye et al. [21] investigated the compression deformation behavior of Al/SiC composites with different contents of SiC_p [20] and particle sizes [21] at different strain rates. Sajjadi et al. [22] found that the compression strength is increased with increasing reinforcement content. The deformation behavior at elevated temperatures was also investigated in many studies [23–28], since required AMC properties and microstructures are often generated by the thermo-mechanical treatment of semi-finished AMC products.

It is well known that the work hardening effect during compression is, in general, significantly reduced at higher deformation temperatures. This results from the thermal activation of micromechanical processes, e.g., dislocation climb and cross slip. In addition, dynamic recovery (DRV) and dynamic recrystallisation (DRX) lead to an enhanced softening effect. DRV can be described as follows: with increased deformation temperature and low strain rate, the dislocation density decreases and the sub-grain boundaries are stronger developed [24]. Therefore, large angle grain boundaries are formed and the sub-grain size gradually increases. These tendencies can be attributed to the resulting higher thermal activation energy and the sufficient time required (for low strain rates) to rearrange the dislocations and ensure sufficient migration of the atoms, which results in flow softening [24]. According to Khodabakhshi et al. [29], who investigated Al matrix hybrid nanocomposites, the relatively high stacking fault energy of Al and its alloys in the low temperature range should facilitate the development of a subgrain structure within (high-angle) grain, which is typical for DRV. In addition to DRV, a microstructure of fine recrystallized grains with a high proportion of high-angle grain boundaries can also be formed during the deformation at higher temperatures [29]. In the progress of this DRX, new grains are permanently formed to compensate for the new, continuously generated dislocations. This dynamic mechanism is commonly observed in hot working at temperatures above 50% of the melting temperature [30]. Concerning the discussion about the materials' behavior at elevated temperatures, dynamic precipitation (DP) also needs to be considered [29,31]. DP follows a similar sequence as static precipitation and also depends on the temperature [32]. It is a diffusion-driven process supported by vacancies and dislocations [33]. The dislocations are favored nucleation sites for precipitates. As a result of dislocation movement during deformation, a homogeneous and dense distribution of very fine precipitates, which contribute to the high strength and hardness values, can be observed [34].

The deformation behavior of AMCs has been studied for a wide range of compositions. Varied material parameters were both matrix material and reinforcement phase (in terms of size, chemical composition and volume content). Though studies were conducted for a wide range of temperatures and strain rates, they usually considered AMCs with a

reinforcement grade of typically below 20 vol% [23–25,28] or with wrought aluminum matrix alloys [26,27]. In the present study, the mechanical properties and microstructural evolution are investigated for a SiC_p/A357 AMC with high reinforcement grade and coarse fraction (35 vol.%, $d_{50} = 21 \mu\text{m}$), suited for high-wear applications. Mechanical tests are conducted under compressive load at room temperature and at 350 °C and compared to the unreinforced A357. In addition, the (combined) effect of two types of reinforcement phase is investigated. Firstly, it is the dispersed SiC_p phase, and secondly a static as well as dynamic precipitation reinforcement. Special focus is placed on DRX behavior and particle fracture during deformation, which are important factors that determine the mechanical properties of the AMC after a possible secondary thermo-mechanical processing.

2. Materials and Methods

2.1. Materials and Processing

An AlSi7Mg0.6 (EN AC 42.200, see DIN EN 1706 [35]) equal to A357 cast aluminum (see The Aluminum Association) powder from ECKA Granules GmbH (Velden, Germany) with an average powder size d_{50} of 40 μm was used as matrix powder. This gas-atomized powder (spherical shape) was mechanically mixed with 35 vol.% polygonal SiC_p (ESK-SIC GmbH, Ferchen, Germany) in a three-dimensional tumbler mixer (TURBULA; Willy A. Bachofen GmbH, Nidderau-Heldenbergen, Germany) for 10 min. The SiC_p fraction (size: F320) was sieved with a mesh size of 20 μm . A final SiC powder size of $d_{50} = 21 \mu\text{m}$ and a distributional width of 21 μm was achieved. The AMC mixed powder fraction and the as-received A357 powder fraction were consolidated in the solid state to cylindrically shaped samples ($D = 40 \text{ mm}$, $h = 8 \text{ mm}$) by RHS with a sintering furnace KCE FCT-HP D 25-SI (FCT Systeme GmbH, Frankenblick, Germany). During this sintering process, the powder was heated by its own electrical resistance or indirectly by the used graphite tool. Due to the high heating and cooling rates, sintering temperatures close to the solidification temperature as well as the high sintering pressures, the used powder can be consolidated within a very short time in the range of few minutes [36]. Based on expertise from previous investigations [2,37], the sintering process was carried out in a vacuum for 5 min (holding time) at 520 °C and at a sintering pressure of 50 MPa to achieve nearly fully dense bodies (porosity < 1%) within a very short time to avoid microstructural coarsening effects. In addition, some samples were subsequently heat-treated in order to enhance the strength. The corresponding T6 heat treatment consisted of solid solution annealing for 1.0 h at 520 °C, quenching in water and subsequent artificial aging for 2.5 h at 180 °C. Consolidation and heat treatment were carried out as described in more detail in our former study [2].

2.2. Mechanical Testing

For compression tests, cylinders with a diameter of 6 mm were cut from each sintered and heat-treated sample in direction of the sintering pressure by wire eroding. The end faces of the cylinders were machined by face turning to achieve plane surfaces and a final specimen height of 6 mm. The compression specimens were taken at a radial position halfway between the center and the outer diameter of the sintered samples.

All material conditions (as-sintered and T6 heat-treated) were investigated by compression tests at room temperature (RT) and at 350 °C at a quasi-static strain rate of 10^{-3} s^{-1} in a Zwick-Roell 100 kN universal testing device (ZwickRoell GmbH & Co. KG, Ulm, Germany) up to a compression of about 50%. Three tests were performed for each condition at the respective temperatures. To reduce friction during testing, a thermally stable copper paste was applied to the end faces of the specimens.

Inductive heating was used for compression tests at elevated temperatures. The specimen temperature was controlled by a pyrometer measuring the temperature on the lateral surface. This was painted with a non-reflecting black layer to ensure a comparable emission during temperature control. All compression specimens were preheated for about one minute and then held at 350 °C for 5 min before testing.

2.3. Microstructural Analysis

A selection of tested compression test specimens were used for microstructural analysis. The longitudinal and cross sections were prepared using conventional metallographic preparation routines. Optical micrographs were taken with an Olympus GX51 microscope (Olympus Deutschland GmbH, Evident Corporation, Tokyo, Japan) for qualitative microstructural analysis. For quantitative microstructural analysis, the software tool Materials Solution (Olympus Deutschland GmbH, Evident Corporation, Tokyo, Japan; evaluation software: Olympus Stream Motion 2.1) was used. Both sample porosity and SiC particle size distribution were monitored by digital image analysis, using grey scale thresholds that were set manually (i.e., light grey (matrix including eutectic silicon), middle grey (SiC_p) and near-black (pores). To evaluate the porosity, five micrographs were taken and for each of these, an area with a size of 250 μm × 250 μm was analyzed. Ten areas with a size of 100 μm × 100 μm obtained from individual micrographs in the centers of the cross sections were used to determine the SiC particle size distribution. The identified particle sizes correspond to the respective average particle diameters determined from the Materials Solution software. The particle size was classified in fractions with increments of 2.5 μm (see Table 1), starting at 5 μm to avoid an erroneous assignment of eutectic Si phase from the matrix, and ending at 22.5 μm, since only a few coarser particles were detected, whose number were not sufficient for an adequate statistical validation.

Table 1. Classification of the SiC_p size (average particle diameters).

Fraction	I	II	III	IV	V	VI	VII
from size (μm)	≥5.0	≥7.5	≥10.0	≥12.5	≥15.0	≥17.5	≥20.0
to size (μm)	<7.5	<10.0	<12.5	<15.0	<17.5	<20.0	<22.5

Additional electron-backscatter diffraction (EBSD) measurements were carried out on sintered and T6 heat-treated samples as well as compression specimens tested at 350 °C for the material A357. The AMC conditions could not be characterized by EBSD due to the high content of reinforcement particles (35 vol.%), since the SiC_p were considerably harder than the aluminum matrix and protruded from the polished sample surface. Due to the inclination of the sample during EBSD, this resulted in extensive shadowing effects and therefore large areas with unreliable or no information. The embedded samples were manually ground and subjected to the polishing routine given in Table 2. The final vibratory polishing step (5) was carried out for 45 min in an aqueous colloidal silica suspension consisting of 100 mL of distilled water and 50 mL of MasterMet (Buehler GmbH, Leinfelden-Echterdingen, Germany).

Table 2. Polishing routine for EBSD measurements of the A357 alloy.

Step	Polishing Cloth	Polishing Suspension	Contact Force	Duration
(1)	Struers ¹ , Sat	3 μm, diamond	5 N	2 × 3 min
(2)	Struers ¹ , Plus	1 μm, diamond	5 N	2 × 4 min
(3)	Struers ¹ , Chem	0.06 μm, silica	5 N	1 × 3 min
(4)	Struers ¹ , Flocc	0.25 μm, diamond	5 N	4 × 5 min
(5)	Buehler, MasterTex	0.06 μm, silica (diluted)	-	1 × 45 min

¹ Struers GmbH, Willich, Germany.

A Neon 40 EsB field emission SEM (Carl Zeiss AG, Oberkochen, Germany) equipped with a DigiView IV EBSD camera (EDAX Inc., Mahwah, NJ, USA) was used for microstructural characterization. The EBSD patterns were collected at an acceleration voltage of 20 kV with an aperture of 120 μm. The step size for all measurements was 0.1 μm. Post-processing of the raw data in OIM Analysis (EDAX Inc., Mahwah, NJ, USA) software included a slight clean-up based on the neighbor confidence index correlation (CI < 0.05).

2.4. Differential Scanning Calorimetry

The precipitation behavior of selected A357 samples was analyzed using a DSC 1 System (Mettler Toledo AG, Gießen, Switzerland). Therefore, cylindrical specimens with a diameter of 5.0 mm, a height of 5.5 mm and a resulting mass of approx. 255 mg were tested. A high-purity Al5N (99.999% Al) sample was used as the reference. The samples were placed in aluminum crucibles and tested in nitrogen. Heating was carried out at a rate of 20 K/min up to 400 °C with subsequent cooling (20 K/min) to RT. This thermal cycle was iterated twice for baseline correction.

3. Results and Discussion

3.1. Microstructural Characterization of the Sample Conditions before Compression Test

Representative optical micrographs of the RHS-sintered $\text{SiC}_p/\text{A357}$ in both as-sintered and T6 heat-treated condition are presented in Figure 1a,b, respectively. In general, the microstructure of the investigated $\text{SiC}_p/\text{A357}$ is characterized by reinforcing particles (dark grey) surrounded by the aluminum matrix (light grey). Due to the mixed state of the feed powder as well as the short process time of RHS that does not allow strong diffusion, there are some SiC_p agglomerations that locally led to pores (black). In addition, the RHS-sintered matrix material exhibits very fine, evenly distributed eutectic Si of globular shape (see Figure 1a). This particulate phase coarsened during the T6 heat treatment (Figure 1b), as described in [2] for the unreinforced A357 alloy. It was also observed and discussed that the porosity of the sintered material increased during heat treatment [2], which can be confirmed for the AMCs by Archimedeian density measurements (3D) and quantitative microstructure analysis (2D) (see Table 3). The difference to theoretical density was calculated from the determined density values. Therefore, the density was subtracted from the theoretical density (here: $2.67 \text{ g}\cdot\text{cm}^{-3}$ for the unreinforced condition and $2.86 \text{ g}\cdot\text{cm}^{-3}$ for a reinforcement content of 35 vol.% SiC).

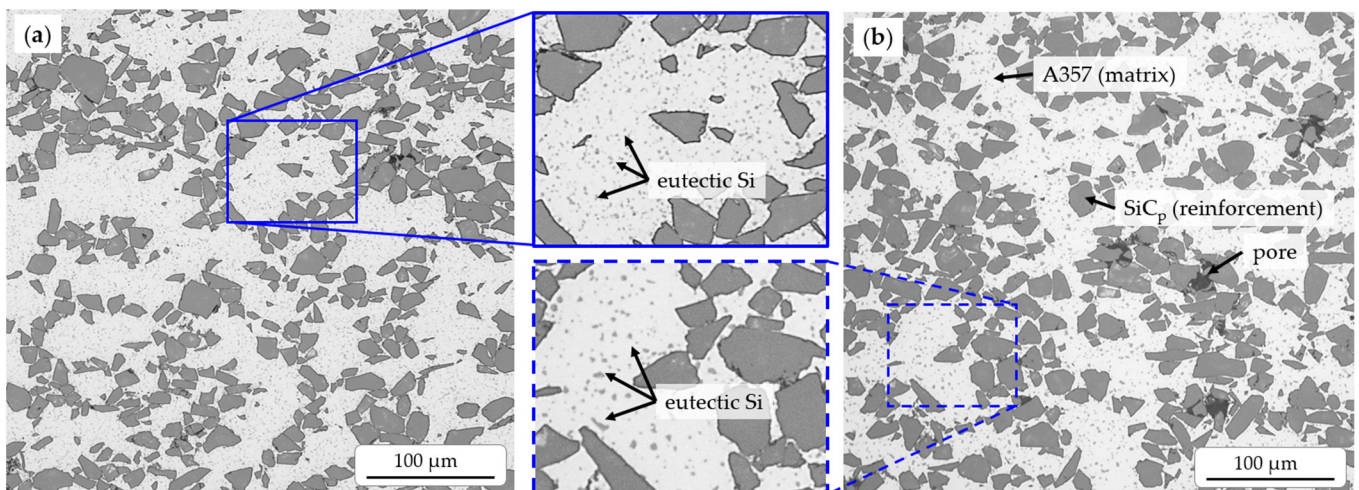


Figure 1. Optical micrographs of the RHS-sintered AMC in the as-sintered (a) and T6 heat-treated condition (b). The eutectic silicon coarsened due to T6 heat treatment (see detail views).

Table 3. The difference in theoretical density and porosity of the investigated materials.

Material	Difference to Theoretical Density (%)		Porosity (%)	
	as-Sintered	T6	as-Sintered	T6
$\text{SiC}_p/\text{A357}$	1.4 ± 0.0	2.1 ± 0.3	0.6 ± 0.3	1.6 ± 0.1
A357	0.1 ± 0.0^1	2.0 ± 0.4^1	0.0 ± 0.0	0.4 ± 0.1

¹ after [2].

It can be assumed that along with the trapped residual gas between former powder particles during sintering [2], argon gas that was trapped in a solid solution during rapid cooling after the gas atomization process (powder manufacturing process) may also have been released during the static (pressureless) solution annealing. Even though the porosity only provides information about the microstructure within the section plane, both the difference to the theoretical density and the porosity show that the initial porosity is higher for the AMCs. However, the increase in the difference to the theoretical density as a result of the heat treatment is stronger for the unreinforced A357 sinter material than for SiC_p/A357, which is due to the higher volume of aluminum alloy in the sintered body. The opposite effect can be observed for the porosity. In general, the quantitative microstructure analyses show smaller values for porosity, which are caused by local differences between the analyzed small areas or volumes, even if a high number of pictures are analyzed and operator influences (e.g., by differently set grey-scale thresholds) can be ruled out. On this basis, the difference to the theoretical density, which gives an average value for a larger sample area or volume, should be preferred. Accordingly, it can be concluded from these results that the materials have a comparable density regardless of the reinforcement. However, for a quantitative evaluation of very small or localized areas, only quantitative microstructure analysis can be considered, see Section 3.4.

In addition to the growth of pores and the coarsening of eutectic silicon, as reported for both investigated materials, the T6 heat treatment also promotes grain growth, as shown in Figure 2 for A357. The color-coded orientation maps were obtained from EBSD measurements on the longitudinal sections of the sintered samples and show fine globular grains for both conditions in contrast to conventionally cast AlSiMg alloys with a grain size of more than a hundred microns (see, e.g., [38]). The grain size increases during T6 heat treatment resulting in an average grain size of about 10 μm in contrast to a size of about 5 μm in the as-sintered condition. The average grain width in AlSiMg processed, e.g., via selective laser melting (or laser powder bed fusion) using powders with a similar initial powder particle size of 40 μm, is in the range of 12 μm to 14 μm [39,40]. However, the structure is often heterogeneous with small amounts of equiaxed grains and mainly columnar grains that can exhibit a strong texture [39,41] due to their directional growth during solidification. In contrast, both conditions, as sintered (Figure 2a) and T6 (Figure 2b), exhibit nearly homogeneous distributions of all crystal orientations, i.e., no texturing of the material occurs during sintering or heat treatment which would be indicated by a large number of grains with a similar color. It is to be noted that the plotted orientation colors correspond to the crystal orientations parallel to the direction of the sintering pressure, i.e., perpendicular to the observed section surface, since this would be the direction where a preferred crystal orientation could be expected first.

3.2. Compressive Behavior at RT

The results of the compressions tests are given in Figure 3. Representative stress–strain curves (Figure 3a) show a significant increase in strength due to particle reinforcement and an additional strengthening effect due to T6 heat treatment. Corresponding values for the true offset yield strength (OYS) at a plastic deformation of 0.2% and the true strength at a plastic deformation of 15% were calculated from the stress–strain curves and are given in Figure 3b for A357 and SiC_p/A357, respectively. Since a definite failure (maximum compression strength) of the specimens was not detectable, the strength at a plastic deformation of 15% was determined as an alternative comparative value. Up to this degree of deformation, there was no visible crack formation at the lateral faces of the compression specimens, and the effect of friction is comparatively low due to lubrication.

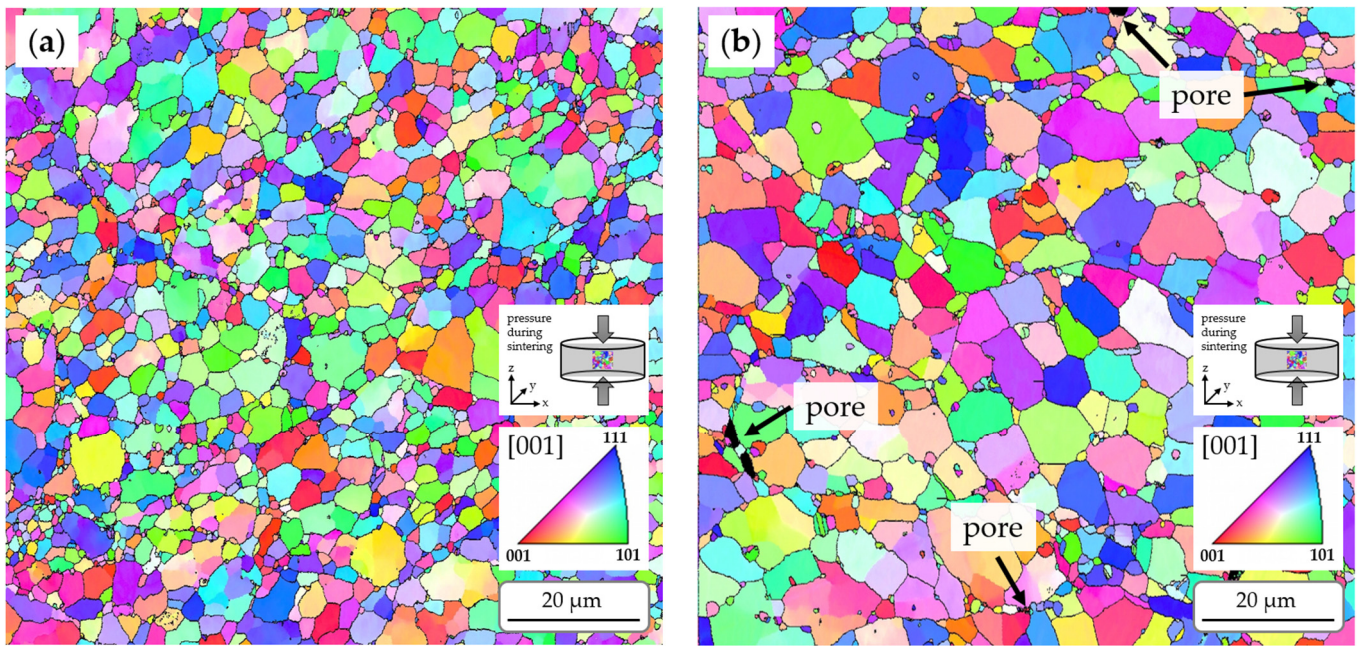


Figure 2. Color-coded orientation maps obtained by EBSD measurements on the longitudinal sections of sintered samples for (a) the as-sintered condition and (b) the T6 heat-treated condition of A357. The colors correspond to the crystal orientation parallel to the sintering pressure, i.e., parallel to the [001] sample direction. High-angle grain boundaries ($>15^\circ$) are marked by black lines.

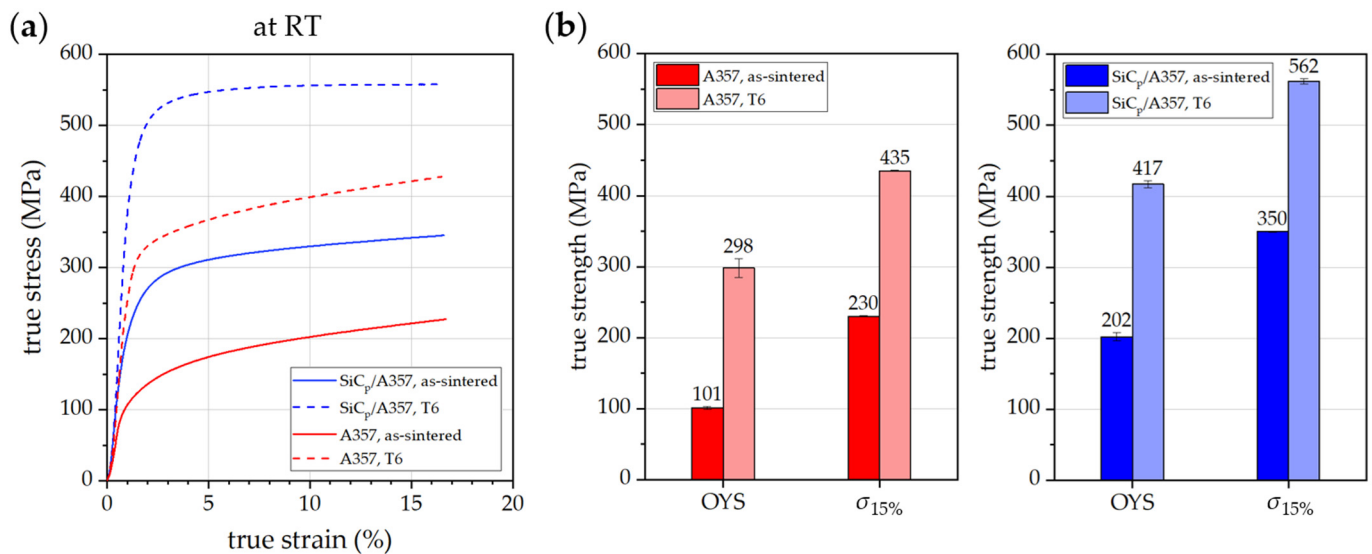


Figure 3. (a) Representative true stress–strain curves plotted up to a true compression of 15% and (b) mechanical properties obtained from compression tests at RT for the as-sintered and T6 conditions.

The as-sintered A357 shows the lowest OYS of about 100 MPa followed by the most pronounced work hardening. By reinforcing (SiC_p/A357), the OYS is doubled. The elastoplastic compressive behavior is characterized by an initially higher rate of strain hardening compared to A357 that decreases after a plastic strain of about 3%. After T6 heat treatment, a similar work hardening behavior can be observed for both materials. However, the strength is increased significantly, i.e., the OYS is higher by about 200 MPa for both A357 and SiC_p/A357. This indicates a relative increase in yield strength of about 200% for A357 and of about 100% for SiC_p/A357. The differences regarding the OYS as well as the work hardening behavior are mainly caused by the dispersion (SiC_p) and/or precipitation hardening (T6) effects. As shown in Figure 3a, T6 heat treatment led to a higher increase in

strength for A357 than a reinforcement with 35 vol.% SiC_p. An additional effect on the onset of plastic flow as well as the work hardening behavior can be expected by pore coarsening and grain coarsening resulting from the T6 heat treatment, see Section 3.1. However, compared to the precipitation hardening, only a minor effect of these microstructural changes can be assumed.

In the following, the investigated material is discussed compared to other particle-reinforced AMCs, taking into account their composition and processing methods: Sankhla et al. [42] also studied the compressive material behavior of AMCs manufactured by powder metallurgy. The composition with pure aluminum and the highest reinforcement content of 25 wt.% of SiC achieved a compression strength of about 260 MPa to 280 MPa. In the case of the sintered material investigated in our study, these values are not yet reached at the onset of yield (OYS), but they are clearly exceeded at a plastic deformation of about 2%. At a plastic deformation of 15%, the strength is higher by about one quarter than that of the pure Al/SiC_p composition. This is mainly due to the higher reinforcement content and alloying elements of our material, which lead to additional strengthening. The compression strength of a stir-cast A356 with a content of 6 wt.% SiC in the T6 heat-treated condition was 334.28 MPa, as investigated by Sunitha et al. [43]. This value is comparable to $\sigma_{15\%}$ of the as-sintered condition of our investigated AMC (Figure 3b), but the value for the T6 condition is even higher by about 70%. Again, the reinforcement content has a significant influence on the strength of the AMC. However, despite the higher volume fraction of age-hardenable aluminum and thus a greater potential amount of strengthening precipitates for the AMC of Sunitha et al. [43], the strength is significant lower. This seems to be contrary considering the strength that can be achieved by the T6 heat treatment (see Figure 3a), even without a reinforcement phase. It should, however, be taken into account, that both materials also differ in terms of Mg content and the manufacturing process which caused a coarser microstructure for the cast AMC [43].

A different ceramic reinforcement was used by Shao et al. [44]. They investigated a cold-sprayed composite with a pure aluminum matrix reinforced with 46 wt.% of Al₂O₃ (≈ 40 vol.%). The maximum OYS achieved for this material was 317.4 MPa. The reinforcement content of the Al₂O₃/Al composite was higher by about 5 vol.% and the porosity was about ten times lower compared to our investigated material SiC_p/A357, which increased the OYS considerably. In addition, the capacity for work hardening was significantly reduced, resulting from an enhanced grain boundary strengthening effect due to the very fine (sub-)grain size of 1 μm or less [44] in the investigated condition that was gained by cold-spray additive manufacturing. As a consequence of the limited plasticity, the maximum strength of the 46 wt.% Al₂O₃/Al was already achieved before a compression of about 2%. In contrast, the grain size of the same material annealed at 500 °C was much coarser (approx. 7 μm on average) and lattice distortion was reduced [44]. Consequently, this heat treatment results in a general reduction in strength but increases the capacity for work hardening during compression. The initial compressive behavior of the annealed AMC is therefore more comparable to the investigated AMC with a similar grain size (see Figure 2). In summary, it can be concluded that not only the AMC composition, but also the manufacturing process and heat treatment affect the mechanical properties significantly.

3.3. Compressive Behavior at 350 °C

The results of the quasi-static compression tests conducted at 350 °C are given in Figure 4. Compared to the tests conducted at RT (Figure 3), the onset of yield (see Figure 4b) is at a significantly lower level of stress, i.e., the OYS of the as-sintered A357 is decreased by about 30% and for the as-sintered SiC_p/A357, the reduction is about 50%. This effect is more pronounced for the T6 heat-treated conditions which exhibit a decrease of about 60% and 70% for A357 and SiC_p/A357, respectively. This considerable reduction in strength arises on the one hand from the lower flow stress at elevated temperatures due to additional thermal activation of dislocation slip and on the other hand from static over-ageing of the T6 tempered samples during heating of the compression samples prior to testing.

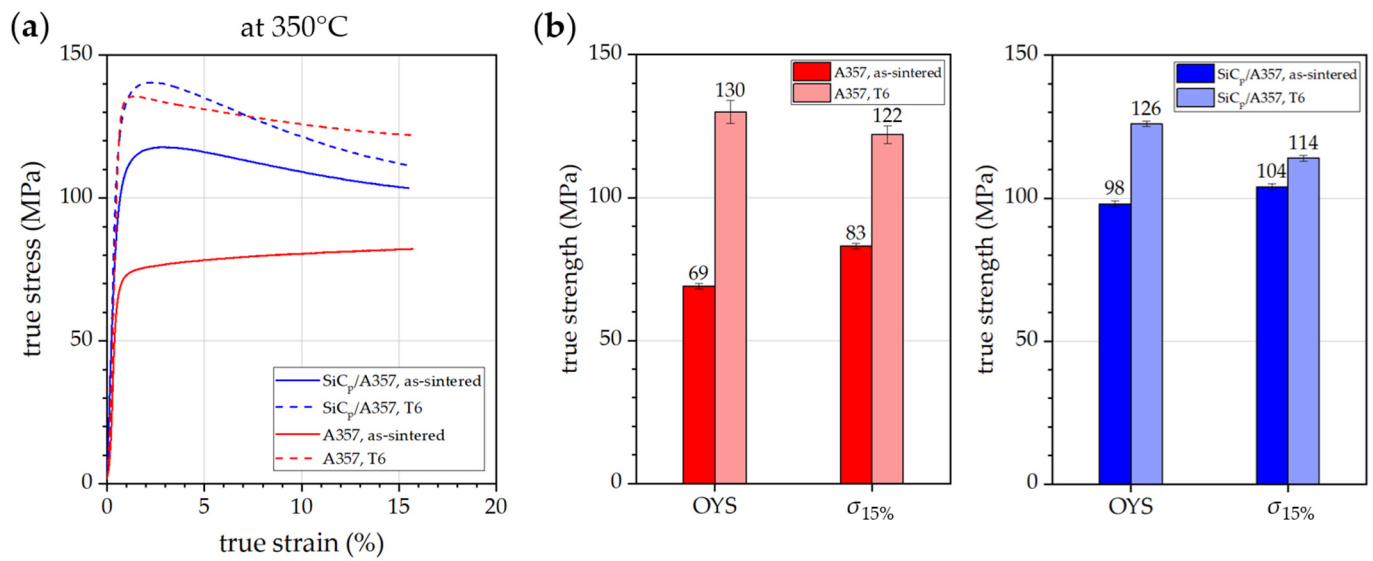


Figure 4. (a) Representative true stress–strain curves plotted up to a true compression of 15% and (b) mechanical properties obtained from compression tests at 350 °C for the as-sintered and T6 conditions.

As shown in the DSC curve of the T6 heat-treated condition of A357 (Figure 5, dashed red line), heating of this sample results in an endothermic peak at temperatures of about 210 °C to 270 °C and a subsequent pronounced exothermic peak with a maximum at about 310 °C followed by an overlapping peak at about 360 °C. These peaks can be assigned to the dissolution of initially present β'' precipitates (II) and the formation of β' precipitates (IV) and β precipitates (V), respectively. As a consequence, these larger β' (coarser, semi-coherent) and β (coarse, incoherent) precipitates hinder the dislocation movement to a lesser extent than the β'' precipitates which results in the lower stress that is necessary for the onset of plastic deformation compared to compression at RT.

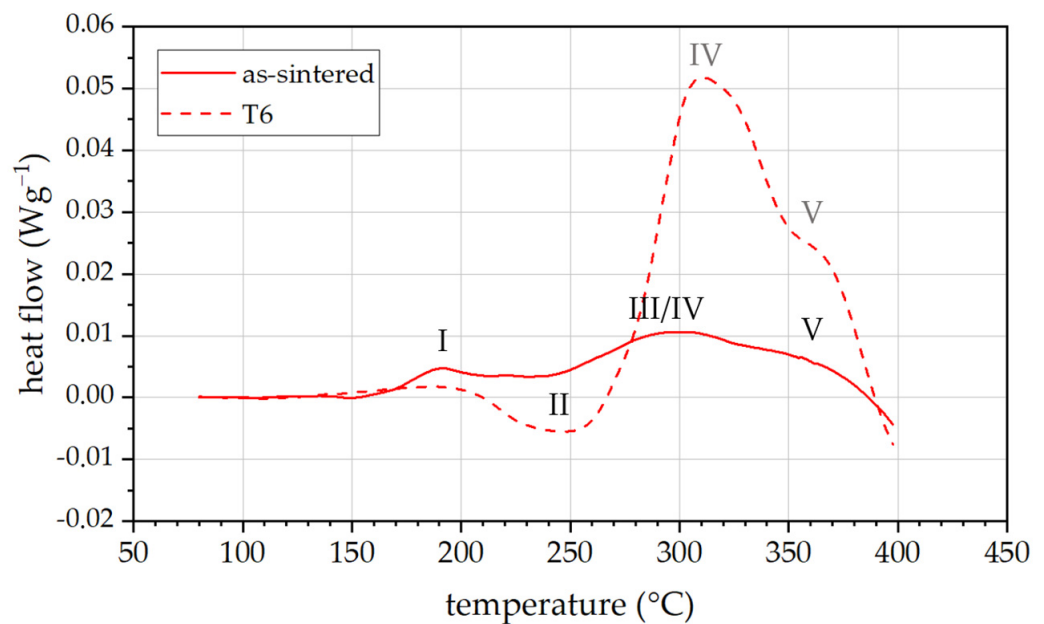


Figure 5. Differential scanning calorimetry (DSC) thermograms of the matrix alloy A357 in the as-sintered condition (solid red line) and T6 condition (dashed red line) obtained at a heating rate of 20 K/min.

In contrast, the DSC curve of the as-sintered condition (solid red line, Figure 5) exhibits only weak, exothermic peaks. This condition is characterized by the temperature progression during the sintering process, i.e., heating and holding at a temperature of 520 °C which can be considered as a suitable temperature for solution annealing and subsequent cooling to RT. Since the cooling rate in this process is not comparable to water-quenching, it can be expected that the atoms that were dissolved during sintering did not remain in the solid solution but already formed precipitates of different stages of the precipitation sequence during cooling. During the subsequent heating (e.g., prior to hot compression testing), these (caused by the low cooling rate) sparsely distributed precipitates grow while their coherency decreases. However, it can be assumed that the precipitation kinetic during testing at 350 °C of the as-sintered conditions starts with the formation of GP I zones at about 190 °C, see Figure 5 (I), which indicates that Si-, Mg- and Mg-Si co-clusters were already present after sintering [9]. This peak is followed by the overlapping formation of β'' (III), β' (IV) and β (V) precipitates, from about 240 °C to 380 °C. At about 380 °C, the precipitation ends and the dissolution of the Mg_2Si phases begins for both conditions. During testing, the temperature is at a level of the formation of the β precipitates (V).

Upon further plastic straining, the stress–strain curves (see Figure 3a) show different trends for the investigated material compositions and conditions. While the strength of the as-sintered A357 is steadily increasing, the other samples exhibit a material behavior typically observed for hot compression [30], i.e., a maximum of strength with a subsequent decrease in the compression stress. This results from additional softening effects initiated at elevated temperatures, namely DRV and DRX, which counteract the strengthening effect of work hardening. Furthermore, the effects of DP need to be considered, which affect the deformation behavior of the as-sintered and T6 heat-treated condition differently, as already discussed in terms of static precipitation during the heating prior to testing.

It can be assumed that the reinforcement and the present precipitations (size and distribution) influence DRV and DRX in a different way for the investigated materials. Regarding the reinforcement, it seems that DRV and DRX are more pronounced for $\text{SiC}_p/\text{A357}$ compared to A357. In general, it is assumed that the reinforcing particles enhance the multiplication and interaction of dislocations during hot deformation and thus promote dynamic recrystallisation [45].

An additional effect on the softening behavior seems to occur for the T6 conditions of both materials. Based on the model of Chen et al. [25], who investigated the hot deformation behavior of a hybrid AMC (micro-SiC and nano-TiB₂), a higher amount of dislocations accumulated at the nano-scaled particles compared to the micro-scaled particles. As a result, these small (incoherent) phases provide a greater driving force for DRX [25]. It can therefore be concluded that (nano-scaled) precipitates also enforce the formation of new grains due to a more continuously increasing pile up and tangle of dislocations [46].

Contrarily, the recrystallisation maps (see Figure 6) of specimens tested up to a deformation of 15% clearly show a higher content of recrystallized grains (blue) for the as-sintered A357, while the corresponding T6 condition is mainly characterized by deformed grains (red) with a higher orientation spread within the grains. This indicates that for the T6 conditions, DRX as well as DRV (low number of yellow, i.e., recovered grains) is inhibited due to a larger number of more regularly distributed precipitates compared to the as-sintered conditions where the spacing between precipitates is expected to be larger. The more regularly dispersed precipitates effectively pin dislocations and promote the dense arrangement of dislocations resulting in a pronounced gradient of misorientation within the grains. Chen et al. [47] furthermore found that the dispersed nanoparticles acted as obstacles for dislocation glide, cross slip and probably climb as well as the migration of low angle grain boundaries and therefore strongly impeded the recovery of the substructures. This confirms the observations in Figure 6b, where only a few small recrystallized grains appear along grain boundaries. The residual microstructure (grain boundaries and substructures) is probably conserved by the network of incoherent precipitates. However, a decrease in strength was noted. On this basis, it can be assumed that the further over-ageing and

coarsening of the precipitates (Ostwald ripening) that was accelerated by the deformation (enhanced dynamic processes) led to the observed softening of the material.

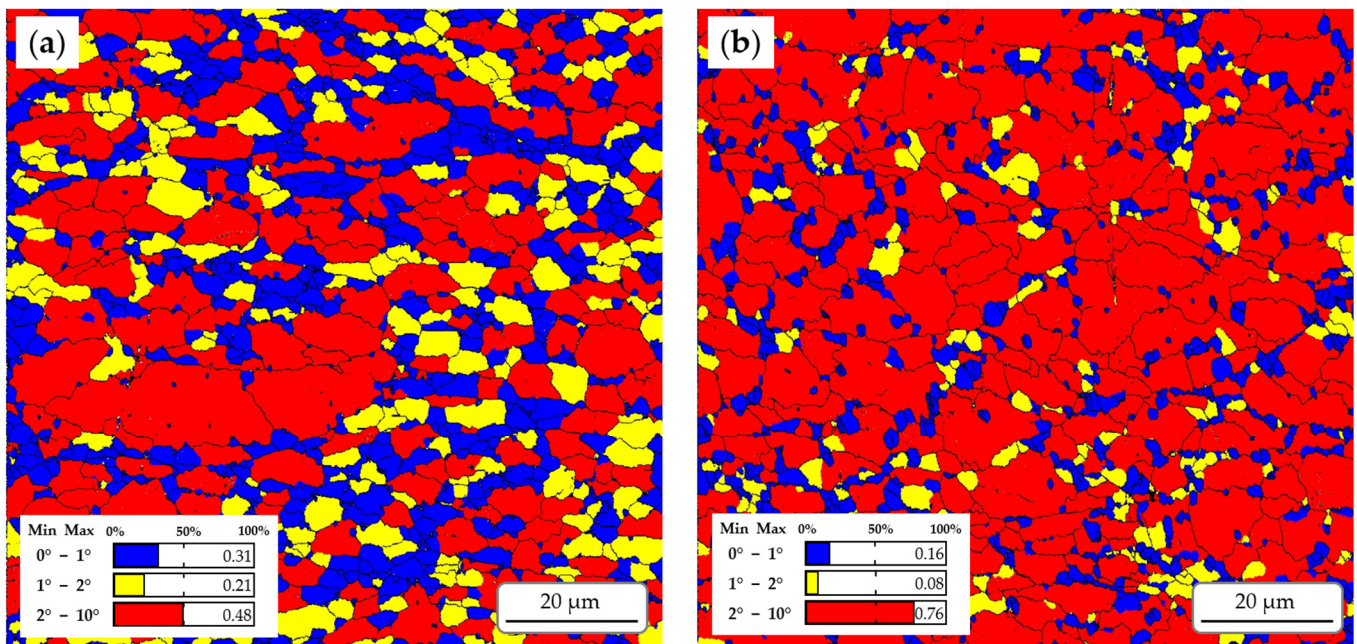


Figure 6. Recrystallisation maps obtained by EBSD measurements on the longitudinal sections of tested (compression ~ 15%) samples for (a) the as-sintered condition and (b) the T6 heat-treated condition of A357. High-angle grain boundaries (>15°) are marked by black lines.

In contrast, the as-sintered condition shows a balance between deformed (red) and recovered or recrystallized (yellow and blue) grains. In this case, the softening effects due to DRV and DRX are more pronounced in comparison to the T6 condition. However, the work hardening of the as-sintered condition is not as strongly reduced as expected. For instance, Liang and Zhang [48], who investigated the flow curves of an Al-Si-Mg alloy similar to A357 at different strain rates and temperatures, found that the flow stress at later stages of deformation still increases when there is insufficient time for stress dissipation (energy accumulation and dislocation annihilation), usually found at higher strain rates. According to the flow curves given in [48,49], there is a peak behavior for compression at 350 °C and at strain rates up to 0.1 s⁻¹. At a strain rate of 1 s⁻¹ and higher, a plateau is observed, which is attributed to a balance between work hardening and dynamic softening. This indicates an additional strengthening effect for the as-sintered A357 in comparison to the T6 condition. Wu et al. [50] found that during hot extrusion the amount of Si particles of cast Al-Si alloys strongly affects the recrystallisation behavior. It is described that with higher Si particles density, more DRX is induced [50]. The Si content of the A357 alloy investigated in our study was not changed, but the density in terms of inter-particle spacing is higher for the as-sintered condition. In addition, the hot compression curves at 350 °C, at the lowest strain rate (10⁻² s⁻¹) determined by Wu et al. [51], show that the smelting-cast near-eutectic Al-Si alloy with finer eutectic silicon has a less pronounced peak behavior than that with coarser Si particles. On the one hand, it can therefore be assumed that the mechanical behavior of the as-sintered condition results from the finer eutectic Si phase distribution (see Figure 1). On the other hand, this is due to the progressive new formation of (strengthening) precipitates, which in turn simultaneously favor the continuous growth of new grains (Figure 6). The rate of strengthening during the compression test continuously decreases (Figure 4a), which is presumably caused by the over-ageing of these new precipitates. This would ultimately result in a softening effect as observed for the T6 condition.

The mechanisms identified for the unreinforced material can presumably be applied to the AMCs. However, the extent of DRX is assumed to be significantly more pronounced

due to the reinforcement [45], resulting in the observed stronger softening. Beside this, an additional reduction in strength was identified by Liu et al. [52]. They found that the reinforcement particles roll and slide within the matrix. Due to this, the particle skeleton becomes more unstable and the deformation behavior is dominated by the matrix [52]. This phenomenon leads to a higher plasticity for the whole composite material compared to deformation at RT. As a consequence, Graf et al. [53] observed an alignment of the reinforcement phase, i.e., an arrangement of the particles corresponding to the direction of material flow. Based on this, the evolution of the microstructure of the AMCs was analyzed and is discussed in detail in Section 3.4.

3.4. Microstructural Evolution of AMCs during Compression

Figure 7 presents optical micrographs of selected specimens tested up to a final compression of 50%. As indicated by the dashed orange ellipses, porosity is slightly reduced but still apparent in the center of the specimen tested at RT, while it is significantly reduced after testing at 350 °C. On the one hand, the high testing temperature led to a reduced flow stress due to thermal activation of dislocation movement and thus enhanced recovery and recrystallisation processes. On the other hand, the strength of the matrix of the T6 condition was additionally reduced by the coarser eutectic Si phase (caused by heat treatment [2]) and over-ageing (reduction in the number of, as well as increase in the spaces between, obstacles for dislocation movement). As a result, lower stresses were necessary to deform the specimen with increasing deformation. For both AMC conditions tested at 350 °C, the final porosity at the specimens' centers, determined by grey threshold values from optical microscopic images, was about $1\% \pm 0.5\%$. Compared to the initial porosity (see Table 3), the reduction in the residual pores is thus more pronounced for the T6 specimens than for the as-sintered specimens tested at 350 °C.

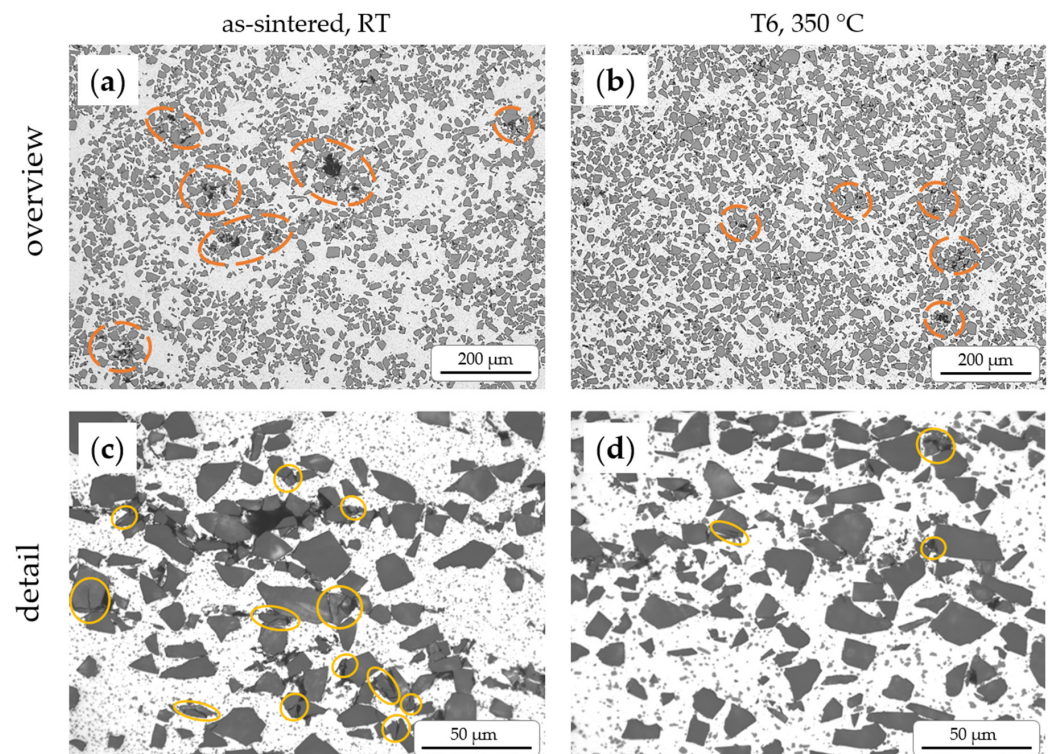


Figure 7. Optical microscopic images of the centers of AMC specimen tested up to a compression of 50% are given as overview (a,b) with the cross-sectional area perpendicular to the compression stress, and in detail (c,d) with the cross-sectional area parallel to the direction of the compression stress. The dashed orange ellipses mark residual porosity and the solid yellow ellipses mark fractured SiC_p which are not incorporated in or surrounded by the aluminum matrix.

In comparison with Figure 1, it also becomes clear that the specimens tested at RT show a similar arrangement of SiC_p , while the distribution of SiC_p became more regular after testing at 350°C for both conditions. Example microstructures are given in Figure 7a,b. In the specimen tested at RT, there are still local areas with more or less accumulated SiC_p caused by the former powder mixture prior to the consolidation process. An opposite effect can be observed for the specimen tested at 350°C . According to Liu et al. [52], the ductile matrix led to an easy sliding and rolling of the particles. In conclusion, this confirms the assumption of a rearrangement favorable for deformation and perhaps also the fast incorporation or surrounding of fractured (see T6 condition) reinforcement particles in or by the matrix during compression.

On a closer look, the qualitative microstructural analysis (see details in Figure 7) and the evaluation of the particle size distribution (see Figure 8) show that during testing at RT the fracture of SiC particles is highest: the contents of particle fractions between IV and VII (from $\geq 12.5\ \mu\text{m}$ to $< 20\ \mu\text{m}$) are significantly reduced and the amount of particles of smaller fractions (I and II, from $\geq 5\ \mu\text{m}$ to $< 10\ \mu\text{m}$) increased compared to the initial condition (Figure 8a,c). To a lesser extent, this can also be observed for the T6 condition tested at 350°C (Figure 8d). Chen et al. [24] and Chen et al. [25] also observed fracturing of the ceramic particles when the stress concentration was higher than the fracture strength of the SiC_p . It is clear that at lower temperatures (here: RT) the stress compensation of the matrix is reduced compared to higher temperatures (here: 350°C), when softening effects, like DRV and DRX, can take place. The probability of damaging the SiC particles is therefore increased for the specimens tested at RT. Unlike the other three conditions, the SiC particle size fractions of the as-sintered condition tested at 350°C is nearly unchanged compared to the initial condition. As found in Section 3.3., different or reduced softening effects took place in the matrix during compression. It was observed that for the as-sintered condition, DRV and DRX were less inhibited due to the absence of a finely distributed precipitation network in comparison to the T6 condition. Therefore, high concentrations of piled-up dislocations could be compensated. As a consequence, nearly no particle fracturing stress concentration occurred during further compression.

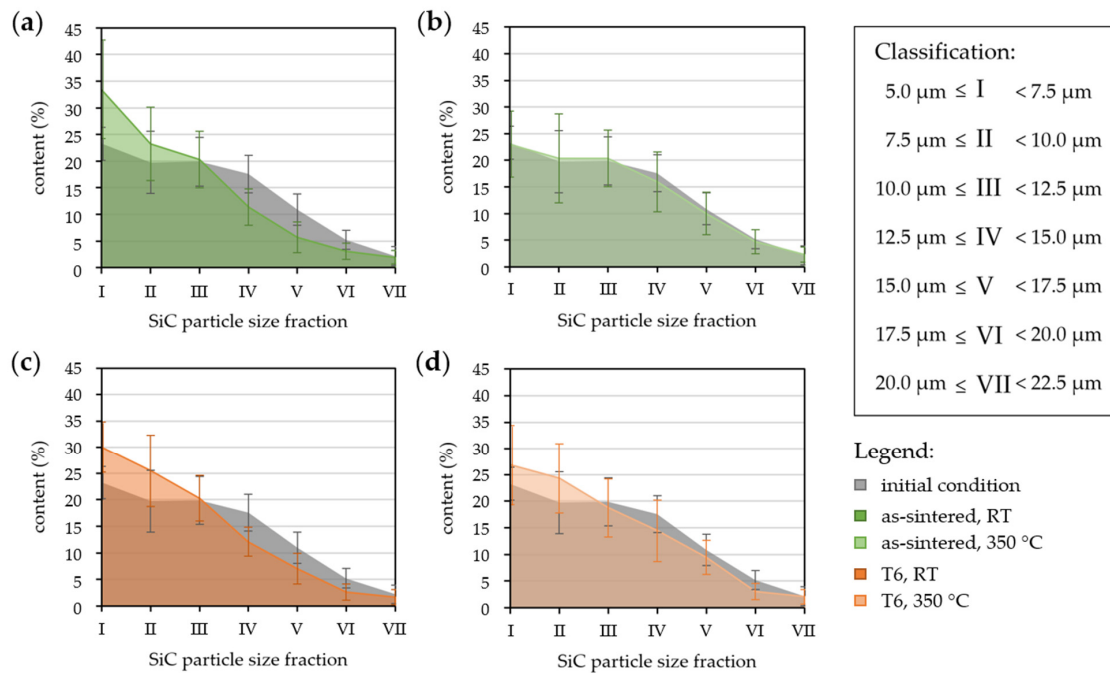


Figure 8. Variation in the SiC particle size distribution before (initial, grey) and after compression tests for the as-sintered ((a)—tested at RT, (b)—tested at 350°C) and T6 heat-treated condition ((c)—tested at RT, (d)—tested at 350°C) after a compression of 50%.

It should be noted that the content of the SiC particle fraction III (from $\geq 10 \mu\text{m}$ to $< 12.5 \mu\text{m}$) is constant before and after testing for all conditions and may therefore be a critical size for the quasi-static compressive deformation of the investigated AMC composition. However, it cannot be clearly separated whether particles of this size are a maximum size for no particle damage or whether particles of this size were formerly a part of bigger particles.

4. Summary

In this study, the compressive behavior of a sintered A357 cast aluminum powder with and without a ceramic particle reinforcement (35 vol.% SiC_p, $d_{50} \approx 21 \mu\text{m}$) was investigated for the as-sintered conditions without subsequent heat treatment as well as for the T6 heat-treated conditions at RT and at 350 °C. The main results are as follows:

- *Testing at RT:*

In general, the addition of reinforcing particles as well as the T6 heat treatment result in an expected increase in strength. However, the strengthening effect of the T6 heat treatment was more pronounced than the effect of particle reinforcement. While the reinforcement led to a doubling of the OYS from about 100 MPa to 200 MPa, the T6 condition led to an increase in OYS by 200 MPa for both materials.

- *Testing at 350 °C:*

Due to softening effects, the strength of all material conditions decreased significantly compared to the RT compression tests. Depending on the initial microstructure (reinforcement particles and precipitates), thermally activated processes like DRV, DRX and DP affect the compressive behavior to varying degrees. It was found that reinforcement generally promotes softening effects, resulting in a pronounced peak behavior in the stress–strain curve. The T6 heat treatment enhances this softening effect by dynamic over-ageing of the already present precipitates. However, for the as-sintered conditions, DP is likely to counteract the softening effects by formation of new precipitates.

In addition, it was observed that SiC particles were fractured during a compression of up to about 50% at RT. At a testing temperature of 350 °C, this effect of particle fracturing is reduced (T6) or even undetectable (as-sintered) which can be attributed to an easier rolling and sliding of the particles within the more ductile aluminum matrix. This additionally led to a rearrangement of the particles.

This more regular distribution of the SiC_p provides the potential for an improved further formability and probably more homogenous properties of the composite with regard to hot forming processes. Furthermore, with regard to wear applications, for which highly ceramic particle-reinforced AMCs are predestined, the more regularly distributed SiC_p could additionally reduce the wear of this material. The potential and significance for processing and application need to be verified by investigations with regard to different application conditions.

Author Contributions: Conceptualization, S.J.H.; methodology, S.J.H.; validation, S.J.H. and N.B.; formal analysis, S.J.H. and N.B.; investigation, S.J.H. and N.B.; resources, T.L.; data curation, S.J.H. and N.B.; writing—original draft preparation, S.J.H. and N.B.; writing—review and editing, T.G. and T.L.; visualization, S.J.H.; supervision, T.G. and T.L. All authors have read and agreed to the published version of the manuscript.

Funding: This research received no external funding.

Data Availability Statement: The authors confirm that the data to support the findings of this study are available within the article.

Acknowledgments: The authors would like to thank Felix Schubert, Steffen Clauß, Mario Scholze and Siddhartha Biswas for their help.

Conflicts of Interest: The authors declare no conflicts of interest.

References

1. Lakshmikanthan, A.; Prabhu, T.R.; Udayagiri, S.B.; Koppad, P.G.; Gupta, M.; Munishamaiah, K.; Bontha, S. The Effect of Heat Treatment on the Mechanical and Tribological Properties of Dual Size SiC Reinforced A357 Matrix Composites. *J. Mater. Res. Technol.* **2020**, *9*, 6434–6452. [\[CrossRef\]](#)
2. Hirsch, S.J.; Winter, L.; Grund, T.; Lampke, T. Heat Treatment Influencing Porosity and Tensile Properties of Field Assisted Sintered AlSi7Mg0.6. *Materials* **2022**, *15*, 2503. [\[CrossRef\]](#) [\[PubMed\]](#)
3. Wang, Q.G. Microstructural Effects on the Tensile and Fracture Behavior of Aluminum Casting Alloys A356/357. *Met. Mater. Trans. A* **2003**, *34*, 2887–2899. [\[CrossRef\]](#)
4. Aversa, A.; Lorusso, M.; Trevisan, F.; Ambrosio, E.P.; Calignano, F.; Manfredi, D.; Biamino, S.; Fino, P.; Lombardi, M.; Pavese, M. Effect of Process and Post-Process Conditions on the Mechanical Properties of an A357 Alloy Produced via Laser Powder Bed Fusion. *Metals* **2017**, *7*, 68. [\[CrossRef\]](#)
5. Zhang, D.; Sun, S.; Qiu, D.; Gibson, M.A.; Dargusch, M.S.; Brandt, M.; Qian, M.; Easton, M. Metal Alloys for Fusion-Based Additive Manufacturing. *Adv. Eng. Mater.* **2018**, *20*, 1700952. [\[CrossRef\]](#)
6. Lathabai, S. Chapter 2—Additive Manufacturing of Aluminium-Based Alloys and Composites. In *Fundamentals of Aluminium Metallurgy*; Lumley, R.N., Ed.; Woodhead Publishing Series in Metals and Surface Engineering; Woodhead Publishing: Duxford, UK, 2018; pp. 47–92. ISBN 978-0-08-102063-0.
7. Zandbergen, M.W.; Cerezo, A.; Smith, G.D.W. Study of Precipitation in Al–Mg–Si Alloys by Atom Probe Tomography II. Influence of Cu Additions. *Acta Mater.* **2015**, *101*, 149–158. [\[CrossRef\]](#)
8. Pogatscher, S.; Antrekowitsch, H.; Leitner, H.; Ebner, T.; Uggowitzner, P.J. Mechanisms Controlling the Artificial Aging of Al–Mg–Si Alloys. *Acta Mater.* **2011**, *59*, 3352–3363. [\[CrossRef\]](#)
9. Winter, L.; Hockauf, K.; Scholze, M.; Hellmig, R.J.; Lampke, T. Influence of Pre-Aging on the Artificial Aging Behavior of a 6056 Aluminum Alloy after Conventional Extrusion. *Metals* **2021**, *11*, 385. [\[CrossRef\]](#)
10. Adebisi, A.A.; Maleque, M.A.; Rahman, M.M. Metal Matrix Composite Brake Rotor: Historical Development and Product Life Cycle Analysis. *Int. J. Automot. Mech. Eng.* **2011**, *4*, 471–480. [\[CrossRef\]](#)
11. Natarajan, N.; Vijayarangan, S.; Rajendran, I. Wear Behaviour of A356/25SiCp Aluminium Matrix Composites Sliding against Automobile Friction Material. *Wear* **2006**, *261*, 812–822. [\[CrossRef\]](#)
12. Daoud, A.; Abou El-khair, M.T. Wear and Friction Behavior of Sand Cast Brake Rotor Made of A359-20vol% SiC Particle Composites Sliding against Automobile Friction Material. *Tribol. Int.* **2010**, *43*, 544–553. [\[CrossRef\]](#)
13. Joshi, Y.G.; Gupta, A.R.; Shingarwade, R.U. Scrutinization of A356/25sipc AMC and Gray Cast Iron as Brake Rotor Material. *Int. J. Res. Advent Technol.* **2014**, *2*, 88–93.
14. Baig, M.M.A.; Al-Qutub, A.M.; Allam, I.M.; Patel, F.; Mohammed, A.S. Tribological Performance of Sub-Micron Al₂O₃-Reinforced Aluminum Composite Brake Rotor Material. *Arab. J. Sci. Eng.* **2021**, *46*, 2691–2700. [\[CrossRef\]](#)
15. Idusuyi, N.; Babajide, I.; Ajayi, O.; Olugasa, T. A Computational Study on the Use of an Aluminium Metal Matrix Composite and Aramid as Alternative Brake Disc and Brake Pad Material. *J. Eng.* **2014**, *2014*, 494697. [\[CrossRef\]](#)
16. Nakanishi, H.; Kakihara, K.; Nakayama, A.; Murayama, T. Development of Aluminum Metal Matrix Composites (Al-MMC) Brake Rotor and Pad. *JSAE Rev.* **2002**, *23*, 365–370. [\[CrossRef\]](#)
17. Chawla, N.; Chawla, K.K. *Metal Matrix Composites*; Springer New York, US, 2006; ISBN 978-0-387-28567-2.
18. Singh, B.; Kumar, I.; Saxena, K.K.; Mohammed, K.A.; Ijaz Khan, M.; Ben Moussa, S.; Shukhratovich Abdullaev, S. A Future Prospects and Current Scenario of Aluminium Metal Matrix Composites Characteristics. *Alex. Eng. J.* **2023**, *76*, 1–17. [\[CrossRef\]](#)
19. Kumar, P.K.D.; Gnanaraj, S.D. Aluminium-Silicon Based Metal Matrix Composites for Brake Rotor Applications: A Review. *Eng. Res. Express* **2023**, *5*, 022002. [\[CrossRef\]](#)
20. Mondal, D.P.; Ganesh, N.V.; Muneshwar, V.S.; Das, S.; Ramakrishnan, N. Effect of SiC Concentration and Strain Rate on the Compressive Deformation Behaviour of 2014Al-SiCp Composite. *Mater. Sci. Eng. A* **2006**, *433*, 18–31. [\[CrossRef\]](#)
21. Ye, T.; Xu, Y.; Ren, J. Effects of SiC Particle Size on Mechanical Properties of SiC Particle Reinforced Aluminum Metal Matrix Composite. *Mater. Sci. Eng. A* **2019**, *753*, 146–155. [\[CrossRef\]](#)
22. Sajjadi, S.A.; Ezatpour, H.R.; Beygi, H. Microstructure and Mechanical Properties of Al–Al₂O₃ Micro and Nano Composites Fabricated by Stir Casting. *Mater. Sci. Eng. A* **2011**, *528*, 8765–8771. [\[CrossRef\]](#)
23. Abouelmagd, G. Hot Deformation and Wear Resistance of P/M Aluminium Metal Matrix Composites. *J. Mater. Process. Technol.* **2004**, *155–156*, 1395–1401. [\[CrossRef\]](#)
24. Chen, S.; Teng, J.; Luo, H.; Wang, Y.; Zhang, H. Hot Deformation Characteristics and Mechanism of PM 8009Al/SiC Particle Reinforced Composites. *Mater. Sci. Eng. A* **2017**, *697*, 194–202. [\[CrossRef\]](#)
25. Chen, X.; Fu, D.; Teng, J.; Zhang, H. Hot Deformation Behavior and Mechanism of Hybrid Aluminum-Matrix Composites Reinforced with Micro-SiC and Nano-TiB₂. *J. Alloys Compd.* **2018**, *753*, 566–575. [\[CrossRef\]](#)
26. Hao, S.; Xie, J.; Wang, A.; Wang, W.; Li, J.; Sun, H. Hot Deformation Behaviors of 35%SiCp/2024Al Metal Matrix Composites. *Trans. Nonferrous Met. Soc. China* **2014**, *24*, 2468–2474. [\[CrossRef\]](#)
27. Hao, S.M.; Xie, J.P. Hot Deformation Behaviors of SiCp/2024 Aluminum Composites. *Adv. Mater. Res.* **2014**, *833*, 271–275. [\[CrossRef\]](#)
28. Kai, X.; Zhao, Y.; Wang, A.; Wang, C.; Mao, Z. Hot Deformation Behavior of in Situ Nano ZrB₂ Reinforced 2024Al Matrix Composite. *Compos. Sci. Technol.* **2015**, *116*, 1–8. [\[CrossRef\]](#)

29. Khodabakhshi, F.; Gerlich, A.P.; Simchi, A.; Kokabi, A.H. Hot Deformation Behavior of an Aluminum-Matrix Hybrid Nanocomposite Fabricated by Friction Stir Processing. *Mater. Sci. Eng. A* **2015**, *626*, 458–466. [[CrossRef](#)]
30. McQueen, H.J. Development of Dynamic Recrystallization Theory. *Mater. Sci. Eng. A* **2004**, *387–389*, 203–208. [[CrossRef](#)]
31. Asgharzadeh, H.; Simchi, A.; Kim, H.S. High-Temperature Deformation and Structural Restoration of a Nanostructured Al Alloy. *Scr. Mater.* **2012**, *66*, 911–914. [[CrossRef](#)]
32. Fan, X.H.; Li, M.; Li, D.Y.; Shao, Y.C.; Zhang, S.R.; Peng, Y.H. Dynamic Recrystallisation and Dynamic Precipitation in AA6061 Aluminium Alloy during Hot Deformation. *Mater. Sci. Technol.* **2014**, *30*, 1263–1272. [[CrossRef](#)]
33. Roven, H.J.; Liu, M.; Werenskiold, J.C. Dynamic Precipitation during Severe Plastic Deformation of an Al–Mg–Si Aluminium Alloy. *Mater. Sci. Eng. A* **2008**, *483–484*, 54–58. [[CrossRef](#)]
34. Teichmann, K.; Marioara, C.D.; Pedersen, K.O.; Marthinsen, K. The Effect of Simultaneous Deformation and Annealing on the Precipitation Behaviour and Mechanical Properties of an Al–Mg–Si Alloy. *Mater. Sci. Eng. A* **2013**, *565*, 228–235. [[CrossRef](#)]
35. *DIN EN 1706*; Aluminium and Aluminium Alloys—Castings—Chemical Composition and Mechanical Properties. Deutsches Institut für Normung: Berlin, Germany, 2021.
36. Hirsch, S.J.; Grund, T.; Lampke, T. Towards Closed-Loop Recycling of Ceramic Particle-Reinforced Aluminium Alloys: Comparative Study of Resistance-Heating Sintered Primary and Solid-State Recycled Secondary SiCp/AlSi7Mg Composites. *Crystals* **2023**, *13*, 830. [[CrossRef](#)]
37. Pippig, R.; Hirsch, S.J.; Grund, T.; Lampke, T. Influence of Metal Matrix Powder Size on the Tensile Strength of a SiCp/AlSi7Mg0.6 Composite Produced by Field Assisted Sintering Technique. *IOP Conf. Ser. Mater. Sci. Eng.* **2021**, *1147*, 012020. [[CrossRef](#)]
38. Fan, H.; Witvrouw, A.; Wolf-Monheim, F.; Souschek, R.; Yang, S. Effects of Substrate Surface Treatments on Hybrid Manufacturing of AlSi7Mg Using Die Casting and Selective Laser Melting. *J. Mater. Sci. Technol.* **2023**, *156*, 142–156. [[CrossRef](#)]
39. Yadav, P.; Rigo, O.; Arvieu, C.; Lacoste, E. Microstructural and Mechanical Aspects of AlSi7Mg0.6 Alloy Related to Scanning Strategies in L-PBF. *Int. J. Adv. Manuf. Technol.* **2022**, *120*, 6205–6223. [[CrossRef](#)]
40. Ming, X.; Song, D.; Yu, A.; Tan, H.; Zhang, Q.; Zhang, Z.; Chen, J.; Lin, X. Effect of Heat Treatment on Microstructure, Mechanical and Thermal Properties of Selective Laser Melted AlSi7Mg Alloy. *J. Alloys Compd.* **2023**, *945*, 169278. [[CrossRef](#)]
41. Hwang, W.J.; Bang, G.B.; Choa, S.-H. Effect of a Stress Relief Heat Treatment of AlSi7Mg and AlSi10Mg Alloys on Mechanical and Electrical Properties According to Silicon Precipitation. *Met. Mater. Int.* **2023**, *29*, 1311–1322. [[CrossRef](#)]
42. Sankhla, A.M.; Patel, K.M.; Makhesana, M.A.; Giasin, K.; Pimenov, D.Y.; Wojciechowski, S.; Khanna, N. Effect of Mixing Method and Particle Size on Hardness and Compressive Strength of Aluminium Based Metal Matrix Composite Prepared through Powder Metallurgy Route. *J. Mater. Res. Technol.* **2022**, *18*, 282–292. [[CrossRef](#)]
43. Sunitha, K.; Gurusami, K.; Rajeswari, N.; Kathikraja, A.; Saravanan, L. Investigation of Mechanical Properties of SiC Particle Reinforced Aluminium A356/LM25 Alloy Composite. *Mater. Today Proc.* **2022**, *66*, 1983–1987. [[CrossRef](#)]
44. Shao, C.; Lo, C.; Bhagavathula, K.; McDonald, A.; Hogan, J. High Strength Particulate Aluminum Matrix Composite Design: Synergistic Strengthening Strategy. *Compos. Commun.* **2021**, *25*, 100697. [[CrossRef](#)]
45. Liu, T.-S.; Dong, B.-X.; Yang, H.-Y.; Qiu, F.; Shu, S.-L.; Jiang, Q.-C. Review on Role of Intermetallic and Ceramic Particles in Recrystallization Driving Force and Microstructure of Wrought Al Alloys. *J. Mater. Res. Technol.* **2023**, *27*, 3374–3395. [[CrossRef](#)]
46. She, H.; Shu, D.; Dong, A.; Wang, J.; Sun, B.; Lai, H. Relationship of Particle Stimulated Nucleation, Recrystallization and Mechanical Properties Responding to Fe and Si Contents in Hot-Extruded 7055 Aluminum Alloys. *J. Mater. Sci. Technol.* **2019**, *35*, 2570–2581. [[CrossRef](#)]
47. Chen, Z.; Sun, G.A.; Wu, Y.; Mathon, M.H.; Borbely, A.; Chen, D.; Ji, G.; Wang, M.L.; Zhong, S.Y.; Wang, H.W. Multi-Scale Study of Microstructure Evolution in Hot Extruded Nano-Sized TiB₂ Particle Reinforced Aluminum Composites. *Mater. Des.* **2017**, *116*, 577–590. [[CrossRef](#)]
48. Liang, Z.; Zhang, Q. Quasi-Static Loading Responses and Constitutive Modeling of Al–Si–Mg Alloy. *Metals* **2018**, *8*, 838. [[CrossRef](#)]
49. Kang, F.; Wei, S.; Zhang, J.; Wang, E.; Fan, D.; Wang, S. Hot Processing Maps and Microstructural Characteristics of A357 Alloy. *J. Mater. Eng. Perform.* **2020**, *29*, 7352–7360. [[CrossRef](#)]
50. Wu, Y.; Liao, H.; Yang, J.; Zhou, K. Effect of Si Content on Dynamic Recrystallization of Al–Si–Mg Alloys During Hot Extrusion. *J. Mater. Sci. Technol.* **2014**, *30*, 1271–1277. [[CrossRef](#)]
51. Wu, Y.; Liu, C.; Liao, H.; Jiang, J.; Ma, A. Joint Effect of Micro-Sized Si Particles and Nano-Sized Dispersoids on the Flow Behavior and Dynamic Recrystallization of near-Eutectic Al–Si Based Alloys during Hot Compression. *J. Alloys Compd.* **2021**, *856*, 158072. [[CrossRef](#)]
52. Liu, B.; Huang, W.; Wang, H.; Wang, M.; Li, X. Compressive Behavior of High Particle Content B4C/Al Composite at Elevated Temperature. *Trans. Nonferrous Met. Soc. China* **2013**, *23*, 2826–2832. [[CrossRef](#)]
53. Graf, M.; Pippig, R.; Lehnert, T.; Jedynak, A.; Härtel, S. Aluminium-Matrix-Composites (AMC) for Hot Forged Components. In Proceedings of the 14th International Conference on the Technology of Plasticity—Current Trends in the Technology of Plasticity; Mocellin, K., Bouchard, P.-O., Bigot, R., Balan, T., Eds.; Springer Nature Switzerland: Cham, Switzerland, 2024; pp. 36–47.

Disclaimer/Publisher’s Note: The statements, opinions and data contained in all publications are solely those of the individual author(s) and contributor(s) and not of MDPI and/or the editor(s). MDPI and/or the editor(s) disclaim responsibility for any injury to people or property resulting from any ideas, methods, instructions or products referred to in the content.